The Astrophysical Journal, 614:1042–1053, 2004 October 20

MAGNETOHYDRODYNAMIC SIMULATION OF SOLAR CORONAL CHROMOSPHERIC EVAPORATION JETS CAUSED BY MAGNETIC RECONNECTION ASSOCIATED WITH MAGNETIC FLUX EMERGENCE

Takehiro Miyagoshi
Kwasan Observatory, Kyoto University, Omine-chou, Kitakazan, Yamashina-ku,
Kyoto 607-8471, Japan; miyagoshi@kwasan.kyoto-u.ac.jp

and

Takaaki Yokoyama
Department of Earth and Planetary Science, University of Tokyo, 7-3-1, Hongo, Bunkyo-ku,
Tokyo 113-0033, Japan; yokoyama.t@eps.s.u-tokyo.ac.jp
Received 2004 February 18; accepted 2004 June 20

ABSTRACT

We studied solar coronal X-ray jets by MHD numerical simulations with heat conduction effects based on a magnetic reconnection model. Key physical processes are included, such as the emergence of magnetic flux from the convection zone, magnetic reconnection with the coronal magnetic fields, heat conduction to the chromosphere, and chromospheric evaporation. Radiation, however, has been neglected. High-density evaporation jets were successfully reproduced in the simulations. The mass of the evaporation jets M is described as $M = 6.8 \times 10^{12}\mathrm{g}(B/10\ \mathrm{G})^{15/7}(T_{\mathrm{cor}}/10^6\ \mathrm{K})^{5/14}(L/5000\ \mathrm{km})^{12/7}(t/400\ \mathrm{s})$, where B is the strength of magnetic fields, T_{cor} is the coronal temperature, L is the loop height, and t is the duration of ejection, respectively. We also derived a theoretical model of the Mach number of the reconnection jets as a function of ambient coronal variables. Numerical simulations also show that two different types of jets (evaporation jets and low-density jets) exist simultaneously around the emerging flux region, and the energy of evaporation jets is somewhat larger than that of the low-density jets.

Subject headings: MHD — Sun: corona — Sun: flares — Sun: magnetic fields

Online material: color figures

1. INTRODUCTION

Yohkoh has revealed the dynamic behavior of the solar corona. One of the most interesting phenomena is "solar coronal X-ray jets" (Shibata et al. 1992; Strong et al. 1992), which are observed as transitory X-ray enhancements with an apparent collimated motion. According to Shimojo et al. (1996; Shimojo & Shibata 2000), the apparent length of the X-ray jets is a few times 10^4 to 4×10^5 km, the velocity ranges from 10 to 1000 km s^{-1} (the average is about 200 km s^{-1}), and the thermal energy of the jets is 10^{27}–10^{29} ergs. Almost all X-ray jets are associated with small flares (subflares, microflares) in X-ray–bright points, emerging flux regions, and active regions. This suggests that both jets and flares have a common physical origin. On the other hand, these small flares have often been thought to be one of the main mechanisms of coronal heating (e.g., Parker 1988; Shimizu 1995; Katsukawa & Tsuneta 2001; Tanuma et al. 2003). Studies of X-ray jets may give us a new viewpoint concerning the heating problem, since the plasma component of the jets may increase the corresponding energy in each flare event.

Shibata et al. (1994) proposed a phenomenological model of the X-ray jets. Based on the frequent observation of X-ray jets from emerging flux regions, they proposed that the plasma in the jets is accelerated and heated by magnetic reconnection between the emerging flux and the preexisting coronal magnetic field. Yokoyama & Shibata (1995, 1996) performed two-dimensional MHD simulations based on this scenario and succeeded in reproducing a plasma-collimated flow along magnetic fields. However, their simulations could not explain the observed density. This is probably because their simulation did not include the effect of conduction and thus evaporation. Shimojo et al. (2001) performed one-dimensional hydrodynamic simulations with conduction effects and succeeded in reproducing the dense flow in X-ray jets under the assumption that the energy input is a given function of time. However, the energy release process (i.e., magnetic reconnection) is not treated in the Shimojo et al. simulation. To study the observed properties self-consistently a combination of the simulations by Yokoyama & Shibata and by Shimojo et al. was needed. Miyagoshi & Yokoyama (2003) extended their work to include the heat conduction effect and chromospheric evaporation process, which were neglected in Yokoyama & Shibata (1995, 1996). The energy release process by magnetic reconnection between the emerging flux the and coronal fields is solved self-consistently in their model; this was neglected in Shimojo et al. (2001) because their work was one-dimensional and energy was given artificially. The key processes of the reconnection model are all included in their model, such as emerging flux from the convection zone, magnetic reconnection to coronal fields, heat conduction to the chromosphere, and plasma evaporation. On the basis of the simulation results, they derived a formula describing the jet mass as a function of the quiet coronal parameters:

$$M = 6.8 \times 10^{12}\ \mathrm{g}\left(\frac{B}{10\ \mathrm{G}}\right)^{15/7}\left(\frac{T_{\mathrm{cor}}}{10^6\ \mathrm{K}}\right)^{5/14} \times \left(\frac{L}{5000\ \mathrm{km}}\right)^{12/7}\left(\frac{t}{400\ \mathrm{s}}\right). \quad (1)$$

In this paper we give a detailed description of the simulation results for self-consistent coronal jets model with emerging

flux, magnetic reconnection, heat conduction, and chromospheric evaporation, which was first reported briefly by Miyagoshi & Yokoyama (2003). We also give a full account of the numerical model that we adopt in the simulations.

This paper is organized as follows. In § 2 the models, assumptions, and basic equations are given. In § 3 the results of numerical simulations and the analysis of them are given. Discussion is given in § 4.

2. MODEL OF NUMERICAL SIMULATIONS

2.1. *A Model of Solar Coronal Jets Based on the Magnetic Reconnection Model*

The basic picture of the magnetic reconnection model by Shibata et al. (1994) is as follows (see Fig. 1): Two antiparallel magnetic field lines of the emerging flux and the preexisting coronal field come close together owing to the rising motion of the emerging flux. By the effect of finite resistivity, they are cut and reconnect with each other. The newly reconnected field lines exert tension force on trapped plasmas, which are accelerated as a result. At the same time, mainly by a slow shock process, magnetic energy is released as thermal energy to heat up the plasma. As a result of these processes, hot plasma is ejected from the reconnection region. The thermal energy of the hot plasma conducts along magnetic fields to the chromosphere because the solar corona is a good heat conductor. This causes "chromospheric evaporation" (Hirayama 1974). There are four key process in the simulations here: emerging magnetic flux, magnetic reconnection, anisotropic heat conduction, and chromospheric evaporation. In order to simulate emerging fluxes, we put a horizontal magnetic flux sheet in the convection zone. The emerging process of the flux sheet is fully reproduced physically (not artificially) by simulating the undular mode of the magnetic buoyancy instability (the Parker instability; Parker 1966). In order to induce magnetic reconnection with this emerging flux, we put a nearly uniform field in the corona. We assume here that the resistivity is anomalous, so that the reconnection takes place violently (Yokoyama & Shibata 1994).

2.2. *Assumptions and Basic Equations*

We solve the nonlinear, time-dependent, resistive, compressible MHD equations. A rectangular computation box with two-dimensional Cartesian coordinates in the x-z plane is assumed ($x_{\min} < x < x_{\max}, z_{\min} < z < z_{\max}$). The surface of the Sun is at $z = 0$. The medium is assumed to be an inviscid perfect gas with a specific heat ratio of $\gamma = 5/3$. Gravitational acceleration is taken into account and is assumed to be uniform in the negative z-direction. An anomalous resistivity model is assumed, as described later. The Ohmic heating and the heat conduction effect are taken into account. The conduction coefficient is a Spitzer-type one that is proportional to $T^{5/2}$, where T is the temperature. We also assume that it is anisotropic, working only in the direction along the magnetic field line, so that $\kappa \approx \kappa_{\parallel} = \kappa_0 T^{5/2}$ (where $\kappa_0 \approx 10^{-6}$ ergs s^{-1} cm^{-1} K$^{-7/2}$) and $\kappa_{\perp} = 0$ in the simulations, where $\kappa_{\parallel}$ and $\kappa_{\perp}$ are the conductivity along and across the magnetic field, respectively. As seen in this, the heat conduction is considered only along the field lines because the perpendicular conductivity $\kappa_{\perp}$ is more than 10 orders of magnitude smaller than the parallel conductivity in the corona (e.g., Priest 1982).

The variables are normalized by quantities related to the initial conditions described below. The units of length, velocity, and time in the simulations are H, C_{s0}, and $\tau \equiv H/C_{s0}$,

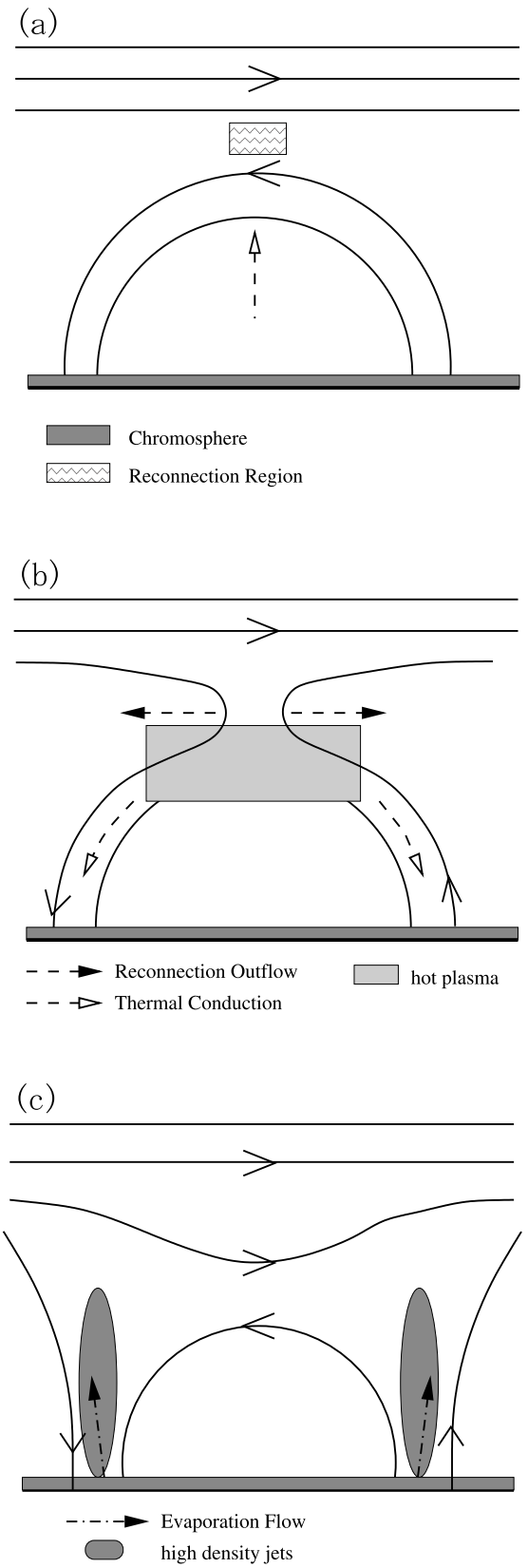

FIG. 1.—Schematic picture of coronal X-ray jets based on magnetic reconnection model. (*a*) The magnetic flux embedded in the convection zone emerges by the Parker instability. (*b*) Interaction occurs between emerging magnetic flux and preexisting coronal fields. Through magnetic reconnection process, the magnetic energy is converted into thermal energy and hot plasma is produced through the shock wave surfaces. This released thermal energy conducts toward the chromosphere along magnetic fields. (*c*) Then, chromospheric evaporation occurs and high-density jet flow is produced.

respectively, where H and C_{s0} are the pressure scale height of the photosphere and the sound speed of the photosphere. Density and temperature are normalized with the initial photosphere values ρ_0 and T_0 at $z = 0$, respectively.

The basic equations are the following:

$$\frac{\partial \rho}{\partial t} + \nabla \cdot (\rho \boldsymbol{V}) = 0, \tag{2}$$

$$\frac{\partial}{\partial t}(\rho \boldsymbol{V}) + \nabla \cdot \left[\rho \boldsymbol{V}\boldsymbol{V} + \left(p + \frac{\boldsymbol{B}^2}{8\pi} \right) \xi - \frac{\boldsymbol{B}\boldsymbol{B}}{4\pi} \right] - \rho \boldsymbol{g} = 0, \tag{3}$$

$$\frac{\partial \boldsymbol{B}}{\partial t} + c \nabla \times \boldsymbol{E} = 0, \tag{4}$$

$$\frac{\partial}{\partial t}\left(\frac{p}{\gamma - 1} + \frac{1}{2}\rho \boldsymbol{V}^2 + \frac{\boldsymbol{B}^2}{8\pi} \right) + \nabla \cdot \left[\left(\frac{\gamma p}{\gamma - 1} + \frac{1}{2}\rho \boldsymbol{V}^2 \right) \boldsymbol{V} + \frac{c}{4\pi} \boldsymbol{E} \times \boldsymbol{B} - \kappa_{\parallel} \nabla_{\parallel} T \right] - \rho \boldsymbol{g} \cdot \boldsymbol{V} = 0, \tag{5}$$

$$p = \frac{k_{\mathrm{B}}}{m} \rho T, \tag{6}$$

$$\boldsymbol{E} = \frac{4\pi}{c^2} \eta \boldsymbol{J} - \frac{1}{c} \boldsymbol{V} \times \boldsymbol{B}, \tag{7}$$

$$\boldsymbol{J} = \frac{c}{4\pi} \nabla \times \boldsymbol{B}. \tag{8}$$

Here ξ is the unit tensor, and ρ, p, $\boldsymbol{V}$, k_{B}, m, and c are the density, pressure, velocity of fluid, Boltzmann constant, mean molecular mass, and light speed, respectively. $\boldsymbol{B}$ is the magnetic field, $\boldsymbol{g}$ ($= -g\boldsymbol{e}_z$, $g =$ const, and $\boldsymbol{e}_z$ is a unit vector in the z-direction) is the gravitational acceleration. The subscript $\parallel$ means that the value is the component parallel to the magnetic field. To solve these equations numerically, they are nondimensionalized with the typical physical values mentioned above.

2.3. *Resistivity Model*

We assumed an anomalous resistivity model (e.g., Sato & Hayashi 1979; Ugai 1992), whose functional form is

$$\eta = \begin{cases} 0 & \text{for } v_d < v_c, \\ \alpha (v_d / v_c - 1)^2 & \text{for } v_d \geq v_c, \end{cases}$$

where α is the nondimensional resistivity parameter, $v_d \equiv J/(en)$ is the (relative ion-electron) drift velocity (e is the elementary electric charge, and n is the particle number density), v_c is the threshold above which anomalous resistivity sets in, and $J = (J_x^2 + J_y^2 + J_z^2)^{1/2}$ is the total current density. The current density J and drift velocity v_d are normalized with the typical values mentioned in § 2.2. The typical current density J_0 is given as $J_0 \equiv cB_0/(4\pi H)$, where B_0 is the typical intensity of the magnetic fields, and B_0 is given as $B_0 \equiv (\gamma n_0 k_{\mathrm{B}} T_0)^{1/2}$, where $n_0 = \rho_0/m$. For example, let us suppose that $T_0 = 10^4$ K, $n_0 = 10^{17}$ cm^{-3}, and $H = 310$ km, respectively. Then, J_0 becomes 0.12 A m^{-2}. Thus, the typical value (normalization unit) of the drift velocity v_d becomes 0.78×10^{-3} cm s^{-1}. We also assumed that there is an upper limit, $\eta_{\max}$, for the resistivity. In this study, we fixed $v_c = 10^3$, $\alpha = 0.01$, and $\eta_{\max} = 1.0$. The normalized value of $v_c(10^3)$ corresponds to 0.78 cm s^{-1} with the typical value mentioned above. The typical value (normalization unit) of the resistivity η is given as $\eta \equiv HC_{s0}$, and becomes 3.6×10^{13} cm^2 s^{-1}. These parameters are all the same as those in Yokoyama & Shibata (1995, 1996). The value of the Spitzer resistivity in the quiet corona ($T \sim 10^6$ K) is about 10^4 cm^2 s^{-1}. So we adopt a higher resistivity value in the current sheet (x-point), which is much thinner than that in the quiet corona. But the important point is that the resistivity is spatially localized. Localized resistivity is a necessary condition for Petschek-type reconnection to occur (e.g., Ugai 1992; Yokoyama & Shibata 1994). In Petschek-type reconnection, the energy release by magnetic diffusion at the resistive point is very small. A large part of the energy release occurs through MHD slow shocks. So, if only Petschek-type reconnection occurs, the overview and released energy by magnetic reconnection are insensitive above a specified value. A detailed discussion about the dependence on the parameters and resistivity model was made by Yokoyama & Shibata (1994).

2.4. *Initial and Boundary Conditions*

The initial conditions for the simulations are as follows. We considered a gas in magnetohydrostatic equilibrium. The gas consists of three layers: from top to bottom, these are a hot layer ($z \geq z_{\mathrm{tr}}$, modeling of corona), a cool layers ($z_{\mathrm{pho}} \leq z \leq z_{\mathrm{tr}}$, the photosphere/chromosphere), and a convection layer ($z_{\min} \leq z \leq z_{\mathrm{pho}}$, the convection zone). We took $z_{\min} = -5.0$, $z_{\mathrm{pho}} = 0.0$, and $z_{\mathrm{tr}} = 8.0$, respectively. The ratio of coronal temperature and photospheric temperature ($T_{\mathrm{cor}}/T_{\mathrm{pho}}$) is 100 in the typical case. The initial temperature distribution in the hot and cool layer is

$$T(z) = T_{\mathrm{pho}} + \left(T_{\mathrm{cor}} - T_{\mathrm{pho}} \right) \times \frac{1}{2} \left[\tanh \left(\frac{z - z_{\mathrm{tr}}}{w_{\mathrm{tr}}} \right) + 1 \right] \text{ for } z > 0. \tag{9}$$

We took $w_{\mathrm{tr}} = 0.5$, $T_{\mathrm{pho}} = 1 (\approx 10^4$ K). In the convection layer, we took

$$T(z) = T_{\mathrm{pho}} - \left(a \left| \frac{dT}{dz} \right|_{\mathrm{ad}} \right) z \text{ for } z_{\min} \leq z \leq 0, \tag{10}$$

where $|dT/dz|_{\mathrm{ad}} \equiv (\gamma - 1)/\gamma$ is the adiabatic temperature gradient and a is the dimensionless constant of order unity. When $a > 1$, this layer becomes unstable for the convective instability (e.g., Priest 1982; for the convective-Parker instability, see Nozawa et al. 1992). We used $a = 2$.

The initial magnetic field comprises two parts: a flux sheet in the convection layer and a nearly uniform field in the hot layer. The direction of magnetic fields of a flux sheet in the convection layer is positive x-direction, and that in the hot layer is negative x-direction, respectively. The intensity of magnetic fields is given by

$$B(z) = \left[\frac{8\pi p(z)}{\beta(z)} \right]^{1/2}, \tag{11}$$

where $\beta(z)$ is the plasma beta (the ratio of gas pressure to magnetic pressure); $\beta(z)$ is divided to two parts:

$$\frac{1}{\beta(z)} = \frac{1}{\beta_1(z)} + \frac{1}{\beta_2(z)}. \tag{12}$$

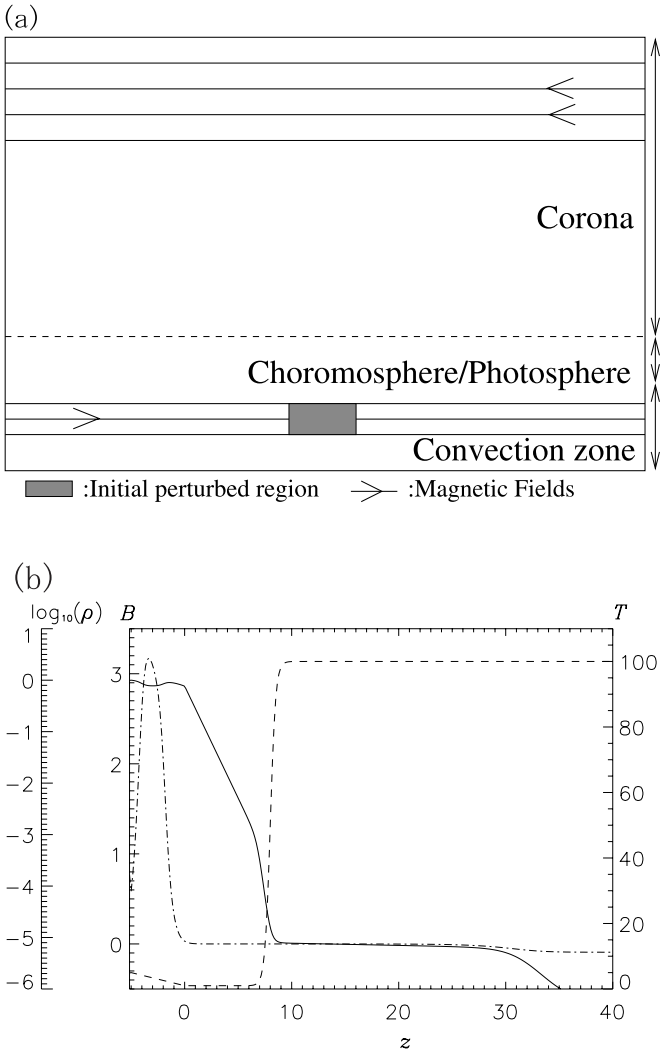

FIG. 2.—(*a*) Schematic picture of an initial magnetic field distribution. The plasma is magnetohydrostatic in the initial phase. A magnetic flux sheet is embedded in the convection zone, and an antiparallel magnetic field is located in the corona. (*b*) The temperature (T; *dashed line*), density (ρ; *solid line*), and the magnetic field (B; *dash-dotted line*) as a function of height z.

Here $\beta_1(z)$ and $\beta_2(z)$ correspond to the flux sheet and the coronal field, respectively. The flux sheet in the convection layer ($z < 0$) is given by

$$\frac{1}{\beta_1(z)} = \frac{1}{\beta_{\rm fs}}\left\{\frac{1}{2}\left[\tanh\left(\frac{z - z_{\rm fsl}}{w_{\rm fsl}}\right) + 1\right]\right\} \times \left\{\frac{1}{2}\left[-\tanh\left(\frac{z - z_{\rm fsu}}{w_{\rm fsu}}\right) + 1\right]\right\}, \quad (13)$$

where $\beta_{\rm fs}$ is the characteristic plasma beta in the magnetic flux sheet. The coronal field is given by $1/\beta_2(z)$. The initial coronal field is horizontal ($B_z = 0$) and is prescribed by

$$\frac{1}{\beta_2(z)} = \frac{1}{\beta_{\rm cor}}\left\{\frac{1}{2}\left[\tanh\left(\frac{z - z_{\rm mgc}}{w_{\rm mgc}}\right) + 1\right]\right\}, \quad (14)$$

where $\beta_{\rm cor}$ is the plasma beta of the coronal field, and $z_{\rm mgc}$ represents the heights of the lower boundary of the field. We took $\beta_{\rm fs} = 4$, $z_{\rm fsl} = -4$, $z_{\rm fsu} = -2$, $w_{\rm fsl} = w_{\rm fsu} = 0.5$, $\beta_{\rm cor} = 0.1$, $w_{\rm mgc} = 2.75$, and $z_{\rm mgc} = 35.0$, respectively. The schematic picture of the initial configuration of magnetic fields is given in Figure 2*a*.

On the basis of the above given functions of temperature $T(z)$ and plasma beta $\beta(z)$, the distributions of the density $\rho(z)$, the pressure $p(z)$, and the magnetic field intensity $B(z)$ were derived by solving numerically the one-dimensional magnetohydrostatic equation in the z-direction:

$$\frac{d}{dz}\left[p(z) + \frac{B^2(z)}{8\pi}\right] + \rho(z)g = 0, \quad (15)$$

with the aid of equations (6) and (11). Figure 2*b* shows the temperature, the density, and the magnetic field strength as a function of height z.

In order to excite the Parker instability (e.g., Parker 1966), a small velocity perturbation of the form

$$V_z = A\cos\left\{2\pi\frac{x - [(x_{\rm max} + x_{\rm min})/2]}{\lambda_p}\right\}, \quad (16)$$

was imposed on the magnetic-flux sheet within finite domain $\left[(x_{\rm max} + x_{\rm min})/2 - \lambda_p/4 < x < (x_{\rm max} + x_{\rm min})/2 + \lambda_p/4\right]$, where A is the amplitude of the perturbation, and λ_p is the wavelength of it, respectively. We took $A = 0.05$ and $\lambda_p = 20$, which is nearly the most unstable wavelength of the linear Parker instability.

In the numerical procedures, the modified Lax-Wendroff method is used for the MHD part of the calculations, and the red and black overrelaxation method is adopted for the anisotropic heat conduction part (e.g., Hirish 1989, p. 476; Yokoyama & Shibata 2001). The number of grid points is 550×500. We adopt nonuniform-scale-sized grid. The minimum grid sizes are $\Delta x = 0.25$ and $\Delta z = 0.15$. For the boundaries, we assumed a periodic condition for $x = x_{\rm min}$ and $x = x_{\rm max}$, a symmetric (rigid conducting wall) condition for $z = z_{\rm min}$, and a free condition for $z = z_{\rm max}$. Here $x_{\rm min} = 0$, $x_{\rm max} = 390$, $z_{\rm min} = -5$, and $z_{\rm max} = 265$, respectively.

3. RESULTS

3.1. *Overview*

Figure 3 shows simulation results. Figures 3*a*, 3*b*, and 3*c* show the time development of density (*color map*), magnetic lines of force (*white lines*), and velocity fields (*white arrows*). Initially, the magnetic flux in the convection layer rises as a result of the Parker instability and evolves to form magnetic loops in the atmosphere (Figs. 3*a* and 3*b*). The loop size is about $L \sim 30 (\sim 5400$ km), which is comparable to the most unstable wavelength of the linear Parker instability (Nozawa et al. 1992). A gravitational downflow occurs along the rising loops (e.g., Shibata et al. 1989). When the top of the rising loops reaches the level of the coronal fields, a current sheet is created between the loop top and the coronal field. We note that reconnection does not immediately occur since there is dense gas carried up with rising loops from the chromosphere and the critical condition for the anomalous resistivity, $v_d \equiv J/\rho > v_c$, is still not satisfied. We also note that the loops are decelerated by coronal pressure. This is because the magnetic pressure at the top of the expanding magnetic loops becomes comparable to the total (gas and magnetic) pressure. As the emerging motion continues, the current sheet becomes thinner and current density increases. Then magnetic reconnection starts when the critical condition for the anomalous resistivity is satisfied. This is the Petschek-type reconnection (e.g.,

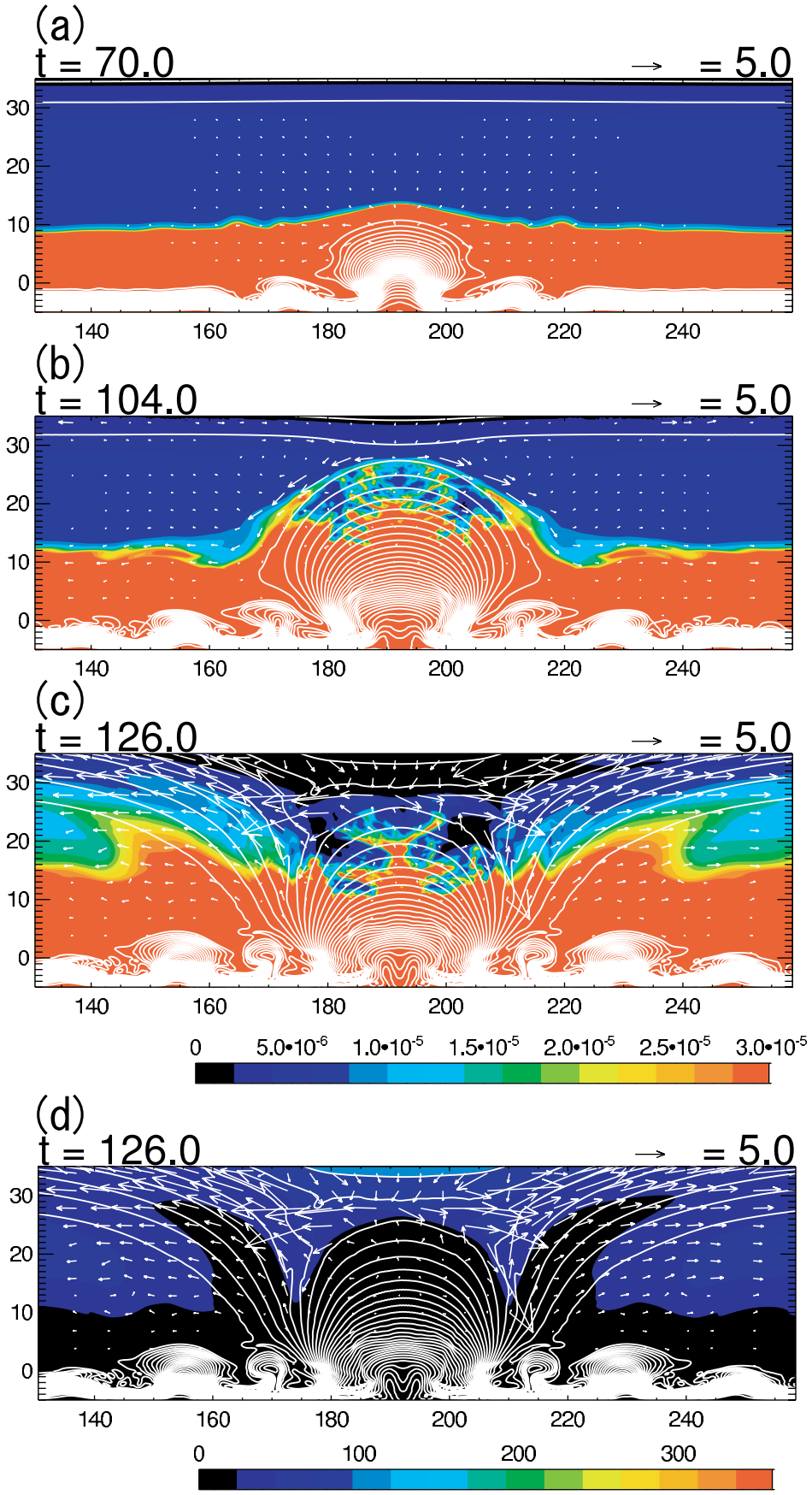

FIG. 3.—Numerical simulation results. The color map shows density (*a*, *b*, and *c*) or temperature (*d*), white solid lines show magnetic lines of force, and white arrows show velocity fields.

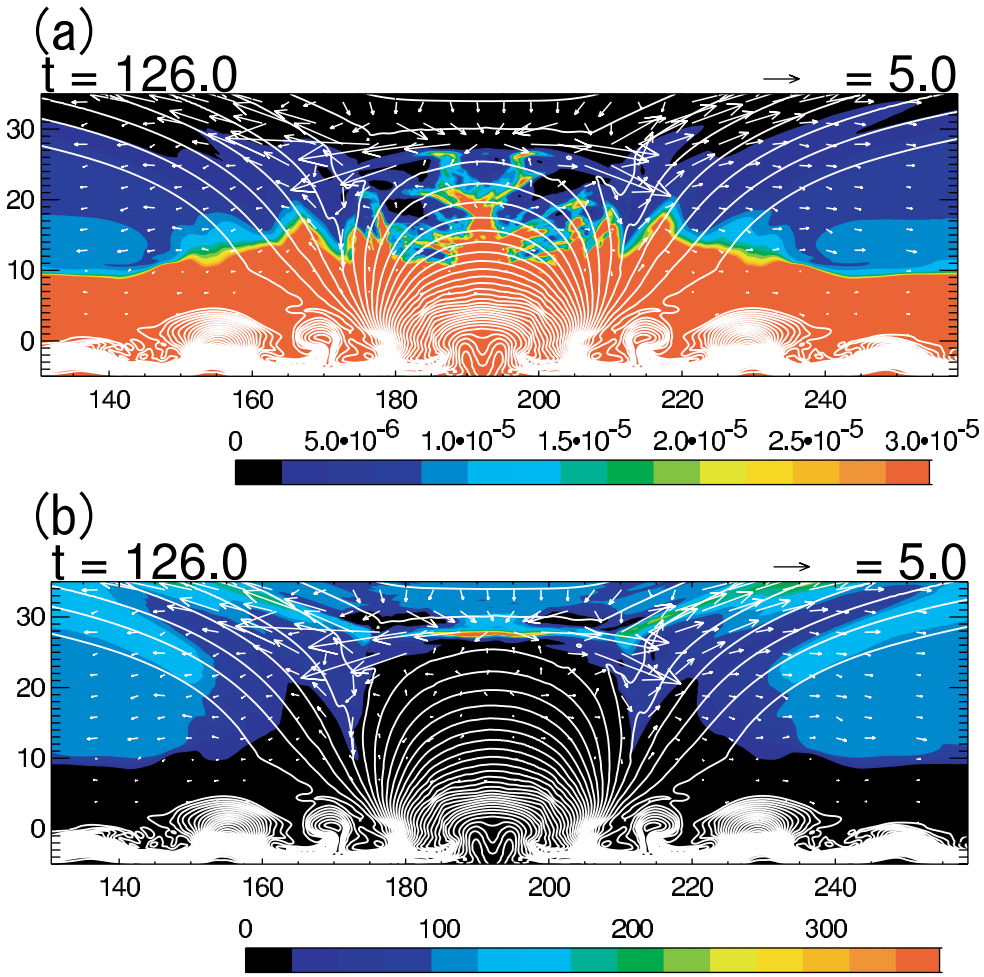

FIG. 4.—Simulation results without heat conduction effect. (*a*) Density map; (*b*) temperature map. Other symbols are as in Fig. 3. In this case, magnetic reconnection occurs but no dense jet flow is formed.

Petschek 1964; Yokoyama & Shibata 1994) because the diffusion region is spatially localized and high-temperature plasma is produced by slow shocks. Magnetic energy is converted into thermal energy through shocks. Then the thermal energy is transported to the chromosphere along the magnetic fields by heat conduction. It causes "chromospheric evaporation" (e.g., Hirayama 1974). The dense gas of the chromosphere rises up along the reconnected magnetic flux by evaporation, and a pair of jets are ejected in the left and right directions (Fig. 3*c*). Figure 4 shows numerical simulation results without heat conduction effects. From comparison of Figure 4 with Figure 3, it is found that the heat conduction effect is essential to reproduce the high density jets.

It is noted that by including the heat conduction effect, the temperature of the reconnection region becomes lower than that of the quiet corona. So this simulation succeeded in reproducing the enhancement of the density but failed to reproduce the enhancement of the temperature in the observed jets (Shimojo & Shibata 2000). The reason for the low temperature is that the cooling by conduction is more efficient than the heating by magnetic reconnection. However, if magnetic field is as strong as that of the real corona, the thermal energy released by magnetic reconnection may increase and, in consequence, the heating rate becomes larger than the cooling rate and temperature should be higher.

3.2. *Mass of the Jets*

Figure 5 shows the total mass of the evaporated plasma a function of coronal parameters. The studied parameters are the coronal magnetic field strength B (Fig. 5*a*), the conduction coefficient κ_0 (Fig. 5*b*), and the initial coronal temperature $T_{\rm cor}$ (Fig. 5*c*). From these results, it is found that the evaporated mass is described as

$$M \propto \kappa_0^{0.3} B^{2.2} T_{\rm cor}^{0.5}, \tag{17}$$

by minimizing the χ^2 error statistic. Note that although κ_0 itself is a universal constant, its value changes in simulations as the normalization unit changes.

This result can be explained as follows. Using the balance between the conductive flux and the enthalpy flux, it is written as

$$\frac{\kappa_0 T^{7/2}}{L} \sim \frac{\gamma}{\gamma - 1} p_{\rm eva} V_{\rm eva}, \tag{18}$$

where T is the temperature of the flare, $p_{\rm eva}$ is the gas pressure of the evaporating plasma, L is the loop height, and $V_{\rm eva}$ is the average velocity of the evaporation flow, respectively. (Note

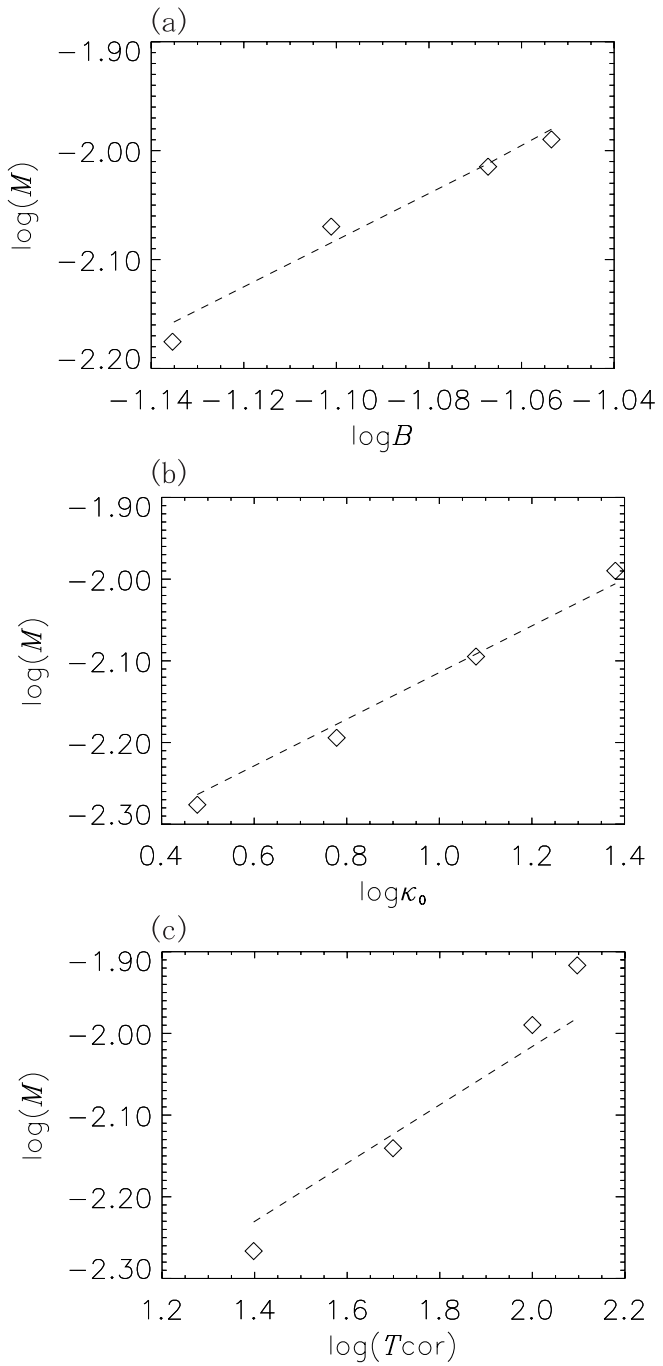

FIG. 5.—Evaporation jet mass (*vertical axis*) as functions of (*a*) magnetic fields strength, (*b*) conduction coefficient, and (*c*) coronal temperature. The diamonds show simulation results, and the dashed line shows the theoretical relation $M \propto \kappa_0^{2/7} B^{15/7} T_{\rm cor}^{5/14}$.

that here we assume that the height of the reconnection region and the loop height are almost equal because reconnection occurs at the loop top.) From this relation and $p_{\rm eva} = (k_{\rm B}/m)\rho_{\rm eva} T$, the mass flux of the evaporating plasma becomes

$$\rho_{\rm eva} V_{\rm eva} \sim \frac{\gamma - 1}{\gamma} \frac{m}{k_{\rm B}} \kappa_0 \frac{T^{5/2}}{L}, \tag{19}$$

where $\rho_{\rm eva}$ is the mass density of the evaporation plasma and $k_{\rm B}$ is the Boltzmann constant, respectively. The temperature of the flare loop is given as follows (e.g., Fisher & Hawley 1990; Shimojo et al. 2001);

$$T \sim (F_h L/\kappa_0)^{2/7}, \tag{20}$$

by the balance between the heating rate and the conduction cooling rate. The heating flux F_h can be regarded as an energy flux into the reconnection region and can be approximated to

$$F_h \sim M_{\rm A} \frac{B^2}{8\pi} V_{\rm A} \sim M_{\rm A} \frac{B^3}{8\pi} \sqrt{\frac{k_{\rm B}}{4\pi m} \frac{T_{\rm cor}}{p_{\rm cor}}}, \tag{21}$$

where $V_{\rm A}$ is the Alfvén speed of the reconnection inflow region, B is the magnetic strength of the corona, $M_{\rm A}$ is the Alfvén Mach number of the reconnection inflow, and $p_{\rm cor}$ is the coronal gas pressure, respectively. If the average velocity of the evaporating plasma and the cross section of the jet are nearly constant in time, the total mass becomes

$$M = \rho_{\rm eva} V_{\rm eva} S t, \tag{22}$$

where S is the cross section of the jet and t is the time from the start of the energy deposition, respectively. Using equations (19), (20), and (21), by eliminating T and F_h, the mass of equation (22) becomes

$$M \sim \frac{\gamma - 1}{\gamma} \frac{M_{\rm A}^{5/7} m^{9/14}}{2 k_b^{9/14} L^{2/7}} \kappa_0^{2/7} B^{15/7} T_{\rm cor}^{5/14} p_{\rm cor}^{-5/14} S t. \tag{23}$$

To compare this analytical model with the simulation results, this is normalized and the formula becomes

$$M' \sim \frac{\gamma - 1}{2\gamma} M_{\rm A}^{5/7} \kappa_0'^{2/7} B'^{15/7} T_{\rm cor}'^{5/14} L'^{-2/7} p_{\rm cor}'^{-5/14} S' t', \tag{24}$$

where the primed values are nondimensional. The dashed lines in Figure 5 indicate this relationship. There is good agreement between the simulations and the analytical model. (Here we express F_h in eq. [21] with $T_{\rm cor}$, not $\rho_{\rm cor}$. This allows for direct comparison between the numerical simulation results and the theoretical model.) The surveyed parameter $T_{\rm cor}$ is a free parameter, so the numerical simulation results shown in Figure 5*c* can be directly compared with equation (24). The density $\rho_{\rm cor}$ is not a free parameter but is automatically determined by equation (15). So we used $T_{\rm cor}$ (and necessarily, $p_{\rm cor}$) instead of $\rho_{\rm cor}$ in equation (21) and thus in equations (23) and (24).

3.3. *Intensity of Fast Shocks and Energetics of Two Types of Jets*

In this process, two regions of energy conversion by shocks exist. They are slow-shock surfaces and fast-shock ones (Yokoyama & Shibata 1996). Dissipation by slow shocks is the main process of conversion from magnetic to kinetic and thermal energy in Petschek-type reconnection. The surfaces of the slow shocks exist near the *x*-point (see Fig. 6). Fast shocks are formed by superfast outflow from the *x*-point accelerated by magnetic reconnection process. Through these two shock surfaces, magnetic energy is released, and then conduction of the converted thermal energy produces evaporation jets. A

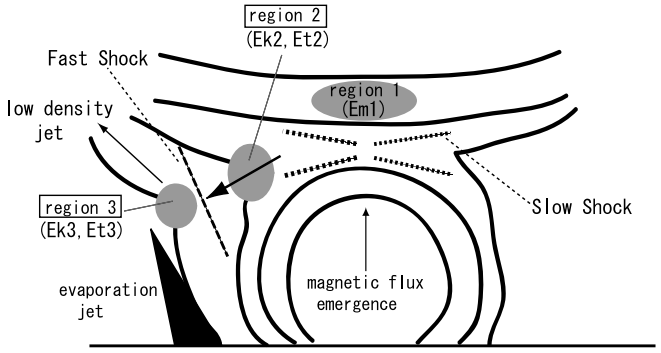

FIG. 6.—Schematic picture of each shock surface location. [*See the electronic edition of the Journal for a color version of this figure.*]

schematic picture of the location of the shock surfaces is shown in Figure 6.

Figure 7*a* shows the Mach number M_f (*vertical axis*) versus the position in the x-direction along $z = 27$ ($170 < x < 215$; Fig. 7*b*, *solid line*). We numbered the region ahead the slow shock surface (i.e., corona) 1, the region behind the slow shock surface 2, and the region behind the fast shock surface 3 (see Fig. 6). Hereafter, these subscripts indicate the region where the physical variables are measured. The shock surfaces located on both sides ($x \approx 176$ and 209) of the x-point are clearly seen as jumps of the Mach number value in Figure 7*a*. The x-point, where outflow velocity is almost 0 and thus $M_f \approx 0$, is also seen at $x \approx 192$ in Figure 7*a*. This is almost the central top of the emerging loop.

Below the intensity of M_f can be understood using the following assumptions: (1) The slow shocks are regarded as switch-off shocks. (2) The fast shocks are approximated as a perpendicular hydrodynamic shock. We can express M_f as

$$M_f^2 = \frac{v_2^2}{C_{s2}^2}, \tag{25}$$

where v_2 is the reconnection outflow speed in region 2 and C_{s2} is the sound speed in the same region. The temperature in region 2 (T_2) is derived from equation (20) and becomes

$$T_2 = \left(\frac{F_h L}{\kappa_0}\right)^{2/7} = \left(M_{\rm A1} E_{m1} V_{\rm A1} \frac{L}{\kappa_0}\right)^{2/7}, \tag{26}$$

by adopting equation (21), where $M_{\rm A1}$ is the Alfvén Mach number in region 1 and $E_{m1} = B_1^2/8\pi$ and $V_{\rm A1}$ are the magnetic energy density and the Alfvén speed in the same region, respectively. The sound speed in region 2 (C_{s2}) becomes

$$C_{s2} = \sqrt{\frac{\gamma k_{\rm B}}{m} T_2} = \sqrt{\frac{\gamma k_{\rm B}}{m}} \left(M_{\rm A1} E_{m1} V_{\rm A1} \frac{L}{\kappa_0}\right)^{1/7}. \tag{27}$$

The kinetic energy in region 2 is about $\frac{3}{5}$ of E_{m1} under assumption 1 (e.g., Priest & Forbes 2000, p. 133), and thus

$$E_{k2} = \frac{1}{2}\rho_2 v_2^2 = \frac{3}{5} E_{m1}. \tag{28}$$

With equations (27) and (28), equation (25) becomes

$$M_f^2 = \frac{6}{5} \frac{m}{\gamma k_b} \frac{E_{m1}^{5/7}/(X\rho_1)}{(M_{\rm A1} V_{\rm A1} L/\kappa_0)^{2/7}}, \tag{29}$$

where $X \equiv \rho_2/\rho_1$ is the compression ratio at the shock. This ratio is given by $X = 1 + (\beta\gamma + \gamma - 1)^{-1} \approx \gamma/(\gamma - 1)$ (e.g., Priest 1982, p. 204) for a low-β switch-off shock with a large angle between the shock normal and magnetic fields. Then the M_f^2 is expressed as

$$M_f^2 = \frac{6}{5} \frac{(\gamma - 1)}{\gamma^2} \frac{m}{k_{\rm B}} \frac{E_{m1}^{5/7}}{(M_{\rm A1} V_{\rm A1} L/\kappa_0)^{2/7} \rho_1}. \tag{30}$$

Equation (30) gives the Mach number of the reconnection jet as a function of coronal variables.

When $B_1 \sim 10$ G, $\rho = 10^9 \times (1.67 \times 10^{-24})$(g cm^{-3}), $M_{\rm A1} = 0.1$, and $\gamma = 5/3$, we obtain $M_f \approx 2.1$ (from numerical simulation results, $M_f \approx 2.0$; see Fig. 7*a*). From the theoretical model (eq. [30]), the relation between M_f and B_1 is expressed as $M_f \propto B_1^{4/7}$. Figure 8 shows the relation between M_f (*vertical axis*) and B_1 (*horizontal axis*) from numerical simulation results (*diamonds*). The dashed line shows the theoretical relation ($M_f \propto B_1^{4/7}$). It is found that there is an agreement in the low-β cases, although a discrepancy is noticeable in the high-β (weak magnetic field) range. The reason is likely to be the following. In the high-β range, X is a function of β, and the approximation of $\beta \ll 1$ is not appropriate. Then, equation (29) becomes a more complex function that includes β. So a discrepancy arises in this high-β range. (The plasma β-values in the corona at the initial state are 0.1, 0.2, and 0.5, respectively in the cases shown in Fig. 8) In the real corona, β is much smaller than 1, so the relation expressed in equation (30) is probably appropriate in the real corona.

Our numerical simulations also show that two types of jets exist simultaneously around the emerging flux region—evaporation jets and low-density jets (see Fig. 7*b*). Evaporation jets have high density and low speed, and the emission measure is large. So they are probably the jets observed by *Yohkoh*. Low-density jets are produced directly by reconnection outflow and flow with high speed. Because of the low emission measure, observation of them is relatively difficult.

The relation between the evaporation jets' energy ($E_{\rm eva}$) and the low-density jets' energy ($E_{\rm low}$) can be explained by considering energy conversion through shock surfaces. Here we define $E_{\rm eva}$ as the energy of high-density jets ($\rho > 1.1 \times 10^{-5}$ in normalized units). We estimate the kinetic energy and thermal energy after considering the energy conversion through these shocks. Here we assume that almost all of the converted thermal energy in the reconnection region (through the slow shock surfaces) conducts along the magnetic loops and is used to produce the evaporation jets, while kinetic energy of the outgoing flow is converted at the fast shock. By using the Rankine-Hugoniot relation, the kinetic energy E_{k3} and the thermal energy E_{t3} behind the fast shock (region 3) becomes

$$E_{k3} = \frac{2M_f^2 + 5}{17M_f^2 + 2} E_{k2}, \quad E_{t3} = \frac{15M_f^2 - 3}{17M_f^2 + 2} E_{k2}. \tag{31}$$

Substituting $M_f = 2.1$ (which has already been derived from eq. [30]) into equation (31), $E_{k3} = (1/6)E_{k2}$ and $E_{t3} = (5/6)E_{k2}$. We assume that half of these energies go to the low-density jet because the flow behind the fast shock is divided into an upward low-density jet and the downward direction. From the above estimations, using equation (28), $E_{\rm low} = (1/2)(E_{k3} + E_{t3}) = (3/10)E_{m1}$ and $E_{\rm eva} = E_{m1} - E_{\rm low} = (7/10)E_{m1}$. So, using the estimation above, the ratio between the evaporation jets' energy and low-density jets' energy, $E_{\rm eva}/E_{\rm low}$, is about 2.3. On

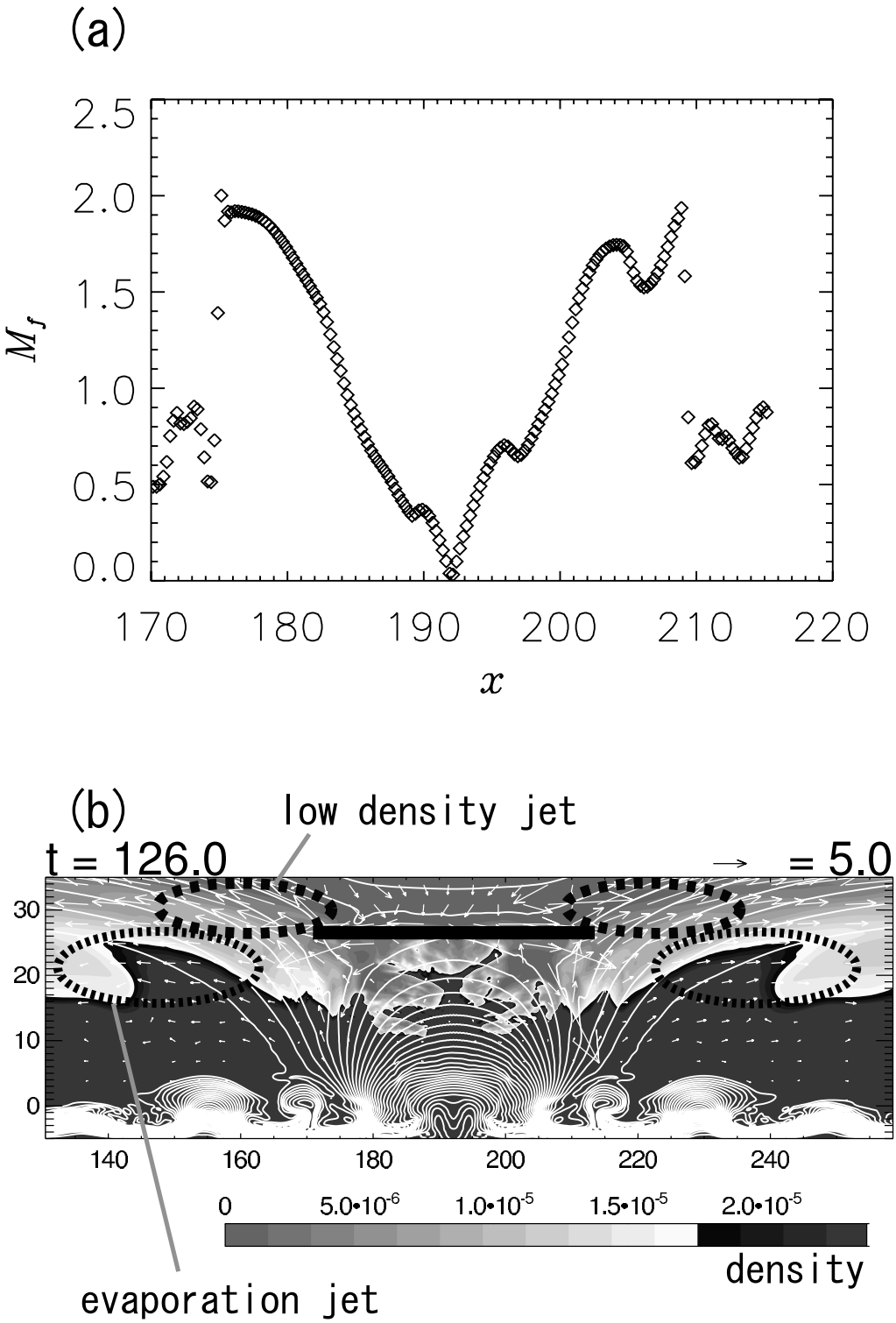

FIG. 7.—(*a*) Mach number M_f (*vertical axis*) vs. x (*horizontal axis, along the solid line shown in b*). (*b*) The location of two types of jets, evaporation jets and low-density jets. [*See the electronic edition of the Journal for a color version of this figure.*]

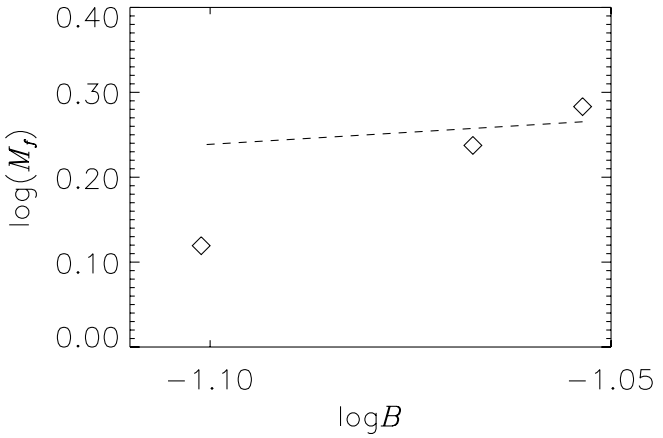

FIG. 8.—Mach number M_f (*vertical axis*) vs. B in the reconnection region (*horizontal axis*). The dashed line shows the relation of $M_f \propto B^{4/7}$.

the other hand, from our numerical simulation results, this value is about 3.5. The slight difference may be caused by other nonlinear effects.

4. DISCUSSION

In this paper we performed MHD numerical simulations of coronal jets that include all the key processes (emerging flux, reconnection, conduction, and evaporation) based on the reconnection model by Shibata et al. (1994). We derived the dependence of the mass of evaporation jets on the coronal variables as equation (23). This is described with typical values of the corona as

$$M = 6.8 \times 10^{12}\ \mathrm{g} \left(\frac{B}{10\ \mathrm{G}}\right)^{15/7} \left(\frac{T_{\mathrm{cor}}}{10^6\ \mathrm{K}}\right)^{5/14} \times \left(\frac{L}{5000\ \mathrm{km}}\right)^{12/7} \left(\frac{t}{400\ \mathrm{s}}\right). \quad (32)$$

Here we assume that the cross section of a jet is approximated as $S \approx L^2$. From observations, the number density in jets is $(0.7\text{–}4.0) \times 10^9$ cm^{-3} and the number density in the footpoint flares is $(2.4\text{–}10.0) \times 10^9$ cm^{-3} (Shimojo & Shibata 2000). From equation (32), the value of the number density in the jet n_{jet} can be derived as $n_{\mathrm{jet}} = M/(2mv)$, where v is the volume of the jet. If the aspect ratio (length over width) of the jet is $\Gamma \sim 7$ (see Shimojo et al. 1996; Shimojo & Shibata 2000), the volume is $v \sim \Gamma L^3 \sim 8.8 \times 10^{26}$ cm^3. Then, we obtain $n_{\mathrm{jet}} \approx 4.5 \times 10^9$ cm^{-3}. This is consistent with the observed values.

From the simulation results, we found that the gas pressure in the jet flow balances with the total (gas and magnetic) pressure of the surrounding gas. Therefore, we consider the jet temperature to be determined by this balance. This balance is described as $p_{\mathrm{jet}} = p_{\mathrm{cor}} + B^2/8\pi$, where p_{jet} is the gas pressure of the jet, p_{cor} is the gas pressure of the outside region, and B is the magnetic field strength of the outside region, respectively. This is because the magnetic pressure in the jets is weak. Let us suppose that $n_{\mathrm{cor}} = 10^9$ cm^{-3}, $T_{\mathrm{cor}} = 10^6$ K, $B = 10$ G, and $n_{\mathrm{jet}} = 4.5 \times 10^9$ cm^{-3}, where n_{cor} is the number density of the outside coronal gas and T_{cor} is the temperature of the outside one, respectively. Using these values and the total pressure balance equation, we get $T_{\mathrm{jet}} = 6.7 \times 10^6$ K, where T_{jet} is the temperature of the jet. This is fairly consistent with the observations (3–8 MK, with an average of 5.6 MK; see Shimojo & Shibata 2000).

The temperature in the reconnection region (and thus that of the low-density jets and evaporation jets) could be high as the strength of the coronal magnetic field increases (this point is briefly mentioned in the last paragraph of § 3.1). This effect can be estimated using equations (20) and (21). By combining equations (20) and (21), we derive

$$T = M_a^{2/7} \left(\frac{B^3 L}{8\pi\kappa_0\sqrt{4\pi\rho}}\right)^{2/7} \approx \frac{1}{2} \left(\frac{B^3 L}{8\pi\kappa_0\sqrt{4\pi\rho}}\right)^{2/7}, \quad (33)$$

where $M_a \approx 0.1$ (this equation is given as eq. (15) in Yokoyama & Shibata 2001). Equation (33) becomes

$$T \approx 3 \times 10^7\ \mathrm{K} \left(\frac{B}{50\ \mathrm{G}}\right)^{6/7} \left(\frac{n}{10^9\ \mathrm{cm}^{-3}}\right)^{-1/7} \left(\frac{L}{10^9\ \mathrm{cm}}\right)^{2/7}. \quad (34)$$

From equation (34), for example, when $B \sim 50$ G, temperature T becomes $T \sim 3 \times 10^7$ K. So several tens of Gauss may be needed to keep the reconnection region at 10 MK.

Our numerical simulations show that the energy of evaporation jets is somewhat larger than that of the low-density jets. We expect that these two quite different types of jets will be observed around the emerging flux region by simultaneous observations with the X-Ray Telescope and EUV Imaging Spectrometer on board *Solar-B*, and that our model will be confirmed by these observations. We also showed that the Mach number M_f ahead the fast-shock surface is expressed as equation (30), which gives the intensity of the fast shock. This estimation can also be applied to the situation of a loop top source region of a flare. We expect that our quantitative estimation, equation (30), will be confirmed by detailed observations of coronal jets and flares by *Solar-B*.

In our model, magnetic reconnection occurs in the corona. We note that the same physical process can occur even below the chromosphere. If the reconnection occurs in the photosphere, we would observe photospheric bright points (e.g., nanoflares), as well as mass flow with a velocity of a few to 10 km s^{-1} (the local Alfvén speed of the photosphere). The wave flux generated by the reconnection could be a source of energy to produce spicules and coronal heating (Kudoh & Shibata 1999).

If we take into account the energy transported by nonthermal electrons, the evaporation becomes more "explosive"—the mass flux of the evaporating plasma becomes much larger, as pointed out by Fisher et al. (1985). This is because the upper chromosphere is unable to radiate the thermal energy deposited there by collision of nonthermal electrons and is therefore heated rapidly to coronal temperatures. This can be checked in the future simulations after taking account of the nonthermal process in the numerical codes.

In this paper we extended the model of Yokoyama & Shibata (1995, 1996) by including anisotropic heat conduction effects. Radiation effects were ignored for simplicity, but this could affect the results. Let us here assume rough estimates of the conduction heating and radiation terms. The conduction heating term C_h is expressed as $C_h = \partial/\partial s(\kappa_0 T^{5/2} \partial T/\partial s)$ ergs s^{-1} cm^{-3}, where s is the distance along the magnetic fields. The radiative-loss term R is expressed as $R = (1/4) n^2 Q(T)$ ergs s^{-1} cm^{-3}, where n is the number density and $Q(T)$ is a function of the temperature T. Here we use the value of $Q(T)$ given in Table 1 of Hori et al. (1997). At $t = 126$ (dense jets were already formed), near $z \sim 20$ ($\sim$6000 km, in the main body of the

evaporation jet), the conduction heating term C_h becomes $C_h \sim 3.6 \times 10^{-2}$ ergs s^{-1} cm^{-3} according to the numerical simulation results, while the radiation term R is estimated to be $R \sim 1.3 \times 10^{-4}$ ergs s^{-1} cm^{-3} with the numerical simulation results ($T \sim 10^6$ K, $n \sim 3 \times 10^9$ cm^{-3}). Near $z \sim 10$ ($\sim$3000 km, near the transition region), the conduction heating term becomes $C_h \sim 1.2 \times 10^{-2}$ ergs s^{-1} cm^{-3} according to the numerical simulation results, while the radiation term is estimated to be $R \sim 6 \times 10^{-1}$ ergs s^{-1} cm^{-3} with the numerical simulation results ($T \sim 5 \times 10^5$ K, $n \sim 10^{11}$ cm^{-3}). At $t = 108$ (the first stage of magnetic reconnection at the loop top), near $z \sim 10$ the conduction heating term C_h becomes $C_h \sim 2.2 \times 10^{-2}$ ergs s^{-1} cm^{-3} according to the numerical simulation results, while the radiation term R is estimated as $R \sim 1 \times 10^{-5}$ ergs s^{-1} cm^{-3} with numerical simulation results ($T \sim 10^6$ K, $n \sim 10^9$ cm^{-3}). Summarizing the above estimates, in the first stage of energy release the radiation term is smaller than the conduction heating term. A short time after evaporation starts, at the base of the jets, the radiation term becomes larger than the conduction heating term because of the evaporated chromospheric cool dense gas. In the main body of the evaporation jet, the conduction heating term is larger than the radiation term.

We also here briefly compare the conduction heating term and the radiation term based on previous works of one-dimensional numerical simulations (e.g., Nagai 1980; Nagai & Emslie 1984; Mariska 1987; Mariska et al. 1989; Fisher 1987; Fisher & Hawley 1990; Krall & Antiochos 1980; Hori et al. 1997). Fisher & Hawley (1990) compare the magnitude of the conduction heating term with that of the radiation term in two stages of a flare by a quasi-analytical method (Figs. 2 and 3 and Appendices A and B in their paper). One is the beginning stage of evaporation (Fig. 2, *bottom*), and the other is the stage after the loop is fully filled with the dense plasma (Fig. 3, *bottom*). At the beginning stage of evaporation, as they mentioned in Appendix A, radiation is thought to affect only the base of the footpoint, while in other places the effect is small (about a few percent of conduction). According to their estimation, the value of the conduction term is larger than that of the radiation term above 2000 km of the loop height. In the upper chromosphere (about a loop height of 3000 km), the conduction term is much larger than the radiation one (about 10–100 times). In the second, strong condensation stage (Fig. 3, *bottom*), this relationship reverses and radiation is larger than conduction up to a loop height of $\sim$6000 km. From the above discussion, it is thought that our equation (32) is applicable in the start stage of evaporation. Krall & Antiochos (1980) also compare the conduction heating term and the radiation term (Fig. 3 in their paper). Although this figure shows the time development of the upper part of the loop (not in the chromosphere), this result is useful for discussing the dynamical variation of the value of the radiation term in evaporation jets propagating to the upper corona in our simulations. According to their result, about 50 minutes after the start of energy deposition, the conduction term value achieves a maximum. Then the conduction term is larger than the radiation term (about $\sim$3 times). After about 80 minutes, the relationship reverses because the chromospheric dense plasma fills up the whole loop. This time interval probably depends on the loop scale (100,000 km in their calculation). These two phases (about 50 and 80 minutes, respectively) may correspond to Fisher & Hawley's two stages. Hori (1998) shows the conductive heating term C_h and radiative loss term R versus the loop height as functions of time t (her Fig. B3). The initial conditions of the numerical simulation are the same as those of Hori et al. (1997). From her result (her Fig. B3), in phase II (beginning of evaporation; a detailed definition is given in Hori et al. 1997), the conduction term is much larger (about $\sim$10,000 times) than the radiation term near a height of 3000 km at $t = 12$ s (at the time when energy deposition starts). In Phase III (when evaporation front reaches the loop top), at $t = 153$, the conduction term is about $\sim$10 times larger than the radiation term near a height of 3000 km, while the radiation term is about half of the conduction term near a height of 1500 km. At $t = 1022$, there is almost an equipartition between radiation and conduction at all heights. Summarizing her result, at the beginning stage of evaporation, the radiation term value is $\sim$1%–10% of the conduction one, but the radiation term increases as time develops, and finally radiation is equal to or larger than conduction heating.

We are grateful to K. Shibata, M. Shimojo, and S. Tanuma for many helpful discussions. We thank D. H. Brooks for many useful comments, especially those that improved the English. We also thank an anonymous referee for his/her helpful comments and suggestions. This work is supported in part by the Grant-in-Aid for the 21st Century COE "Center for Diversity and Universality in Physics" from the Ministry of Education, Culture, Sports, Science and Technology (MEXT) of Japan. This work is also supported in part by the JSPS Japan-UK Cooperation Science Program (principal investigators: K. Shibata and N. O. Weiss). Numerical computations were carried out on a VPP5000 at the Astronomical Data Analysis Center of the National Astronomical Observatory, which is an interuniversity research institute of astronomy operated by Ministry of Education, Culture, Sports, Science, and Technology.

REFERENCES

Fisher, G. H. 1987, ApJ, 317, 502
Fisher, G. H., Canfield, R. C., & McClymont, A. N. 1985, ApJ, 289, 425
Fisher, G. H., & Hawley, S. L. 1990, ApJ, 357, 243
Hirayama, T. 1974, Sol. Phys., 34, 323.
Hirsh, C. 1989, Numerical Computation of Internal and External Flows, Volume 1 (New York: Wiley), 476
Hori, K. 1998, Ph.D. thesis, Tohoku Univ.
Hori, K., Yokoyama, T., Kosugi, T., & Shibata, K. 1997, ApJ, 489, 426
Katsukawa, Y., & Tsuneta, S. 2001, ApJ, 557, 343
Krall, K. R., & Antiochos, S. K. 1980, ApJ, 242, 374
Kudoh, T., & Shibata, K. 1999, ApJ, 514, 493
Mariska, J. T. 1987, ApJ, 319, 465
Mariska, J. T., Emslie, A. G., & Li, P. 1989, ApJ, 341, 1067
Miyagoshi, T., & Yokoyama, T. 2003, ApJ, 593, L133
Nagai, F. 1980, Sol. Phys., 68, 351
Nagai, F., & Emslie, A. G. 1984, ApJ, 279, 896
Nozawa, S., Shibata, K., Matsumoto, R., Tajima, T., Sterling, A. C., Uchida, Y., Ferrari, A., & Rosner, R. 1992, ApJS, 78, 267
Parker, E. N. 1966, ApJ, 145, 811
———. 1988, ApJ, 330, 474
Petschek, H. E. 1964, in Physics of Solar Flares, ed. W. N. Hess (NASA SP-50; Greenbelt: NASA), 425
Priest, E. R. 1982, Solar Magnetohydrodynamics (Dordrecht: Reidel)
Priest, E. R., & Forbes, T. G. 2000, Magnetic Reconnection (Cambridge: Cambridge Univ. Press), 133
Sato, T., & Hayashi, T. 1979, Phys. Fluids, 22, 1189
Shibata, K., Tajima, T., Steinolfson, R. S., & Matsumoto, R. 1989, ApJ, 345, 584
Shibata, K., et al. 1992, PASJ, 44, L173
———. 1994, in Proc. Int. Symp. on the *Yohkoh* Scientific Results, X-ray Solar Physics from *Yohkoh*, ed Y. Uchida et al. (Tokyo: Universal Academy), 29

Shimizu, T. 1995, PASJ, 47, 251
Shimojo, M., Hashimoto, S., Shibata, K., Hirayama, T., Hudson, H. S., & Acton, L. 1996, PASJ, 48, 123
Shimojo, M., & Shibata, K. 2000, ApJ, 542, 1100
Shimojo, M., Shibata, K., Yokoyama, T., & Hori, K. 2001, ApJ, 550, 1051
Strong, K., Harvey, K. L., Hirayama, T., Nitta, N., Shimizu, T., & Tsuneta, S. 1992, PASJ, 44, L161
Tanuma, S., Yokoyama, T., Kudoh, T., & Shibata, K. 2003, ApJ, 582, 215
Ugai, M. 1992, Phys. Fluids B4, 2953
Yokoyama, T., & Shibata, K. 1994, ApJ, 436, L197
———. 1995, Nature, 375, 42
———. 1996, PASJ, 48, 353
———. 2001, ApJ, 549, 1160